Surface Structure Enhanced Microchannel Flow Boiling

Surface Structure Enhanced Microchannel Flow Boiling

Yangying Zhu
Department of Mechanical Engineering
Massachusetts Institute of Technology, Cambridge, MA 02139, USA
yyzhu@mit.edu

Dion S. Antao
Department of Mechanical Engineering
Massachusetts Institute of Technology, Cambridge, MA 02139, USA
dantao@mit.edu

Kuang-Han Chu
Department of Mechanical Engineering
Massachusetts Institute of Technology, Cambridge, MA 02139, USA
flyjohn@gmail.com

Siyu Chen
Department of Mechanical Engineering
Massachusetts Institute of Technology, Cambridge, MA 02139, USA
chensiyu@mit.edu

Terry J. Hendricks
NASA/Jet Propulsion Laboratory
California Institute of Technology, 4800 Oak Grove Drive, Pasadena, CA 91109, USA
terry.j.hendricks@jpl.nasa.gov

Tiejun Zhang
Department of Mechanical and Materials Engineering
Masdar Institute of Science and Technology, P.O. Box 54224, Abu Dhabi, UAE
tjzhang@masdar.ac.ae

Evelyn N. Wang[1]
Department of Mechanical Engineering
Massachusetts Institute of Technology, Cambridge, MA 02139, USA
enwang@mit.edu

[1] Corresponding author

ABSTRACT

We investigated the role of surface microstructures in two-phase microchannels on suppressing flow instabilities and enhancing heat transfer. We designed and fabricated microchannels with well-defined silicon micropillar arrays on the bottom heated microchannel wall to promote capillary flow for thin film evaporation while facilitating nucleation only from the sidewalls. Our experimental results show significantly reduced temperature and pressure drop fluctuation especially at high heat fluxes. A critical heat flux (CHF) of 969 W/cm^2 was achieved with a structured surface, a 57% enhancement compared to a smooth surface. We explain the experimental trends for the CHF enhancement with a liquid wicking model. The results suggest that capillary flow can be maximized to enhance heat transfer via optimizing the microstructure geometry for the development of high performance two-phase microchannel heat sinks.

***Key words**: Microchannel flow boiling, surface microstructures, flow instabilities, critical heat flux*

1 INTRODUCTION

The increasing power densities in various electronic devices including concentrated photovoltaics, power electronics and laser diodes pose significant thermal management challenges for the electronics industry [1–3]. Two-phase microchannel heat sinks are attractive to cool advanced electronic devices because they harness the latent heat of vaporization to dissipate high heat fluxes in a compact form factor. However, minimizing flow instabilities during boiling while enhancing the critical heat flux (CHF) to maximize heat dissipation has been difficult to achieve [4–6]. These flow instabilities which can be triggered by several mechanisms including explosive bubble expansion [7], upstream compressibility [8,9] and density wave oscillation [10] can lead to large pressure drop fluctuations across the channels and temperature spikes associated with liquid dry-out. This dry-out severely limits the heat removal ability of these microchannel heat sinks and leads to device failure once reaching CHF [11].

To suppress flow instability and to enhance heat transfer, recent studies have focused on incorporating various structures in microchannels, such as inlet restrictors [12–14], artificial nucleation sites [14,15], vapor venting membranes [16–18], micro pin fins [19–21], and nanowire-coated surfaces [22–24] integrated into the microchannel. However, there are challenges with several of these approaches. Inlet restrictors can significantly reduce backflow but with a pressure drop penalty for the stabilization [13]. Fabricated nucleation sites have demonstrated enhanced nucleate boiling heat transfer, however, the introduction of the cavities alone can increase the instabilities [14]. Vapor venting membranes can reduce dry-out and pressure drop oscillations by locally

removing the expanding vapor, however the operational range is limited due to the risk of membrane flooding at high pressures [17].

Micro and nanostructure-coated surfaces are attractive owing to the ability to modify surface wettability, generate capillarity and create nucleation sites. In fact, in pool boiling, superhydrophilic micro and nanostructures have demonstrated significantly increased CHF [25–31] and biphilic patterned surfaces have shown large enhancements in heat transfer coefficients [32,33]. In flow boiling, silicon nanowire-coated channel surfaces have been reported to reduce temperature fluctuations [22], increase the heat transfer coefficient and CHF, and decrease the pressure drop across the microchannels with water as the working fluid [23,24]. The enhancement mechanism was mainly attributed to both increased wettability in delaying CHF and nucleation sites formed by the nanowire bundles to improve the heat transfer coefficient in the nucleate boiling regime. At high heat fluxes, however, the annular flow regime typically dominates, where film evaporation is the important heat transfer mode [4]. Thus the role of the surface structures on the stability of the annular liquid film and on the film evaporation performance needs to be investigated. In addition, while introducing structures on the channel wall offers capillary driven liquid flow, the associated viscous resistance [34–36] from the structures, especially in the presence of shear from the vapor, can be significant. These effects are sensitive to the geometry of the structures. Therefore the precise role of the surface structures on flow boiling needs to be studied in more detail.

In this work, we investigated well-defined superhydrophilic microstructured surfaces in microchannels for flow boiling heat transfer. These surface structures have length scales much smaller than the height of the microchannel, and thus are different

from micro pin fins which extend to the ceiling of the microchannel [19–21]. We fabricated and characterized microchannels with well-defined micropillar arrays on the bottom channel wall, where heat was applied. The hydrophilic micropillars were only integrated on the heated bottom surface to promote wicking and film evaporation while suppressing dry-out. The sidewalls, with tailored roughness of 1-2 μm, promoted nucleation near the bottom corners [37]. Spatially decoupling nucleation to the sidewalls and film evaporation to the bottom surface promises to achieve high heat fluxes while maintaining stable heat transfer performance. We characterized structured surface microchannel and benchmark smooth surface microchannel devices in a custom closed loop setup. In particular, we investigated flow instabilities through temporally resolved temperature and pressure drop measurements, and simultaneous visualization of the flow in the device. We also characterized the heat transfer performance (the heat transfer coefficient, the CHF and the pressure drop), and explained the experimental trends for the CHF enhancement with an adiabatic liquid wicking model. The insights gained from this work are a first step towards guiding the design of stable, high performance surface structure enhanced two-phase microchannel heat sinks.

2 METHODOLOGY

In high heat flux applications, microchannel heat sinks usually operate in the annular flow regime due to the high vapor quality associated with heat dissipation in the confined space [38]. Since evaporation can be dominant in the annular flow regime, we designed the structured surfaces to enhance and sustain stable liquid film evaporation (Figure 1a and 1b). The structures were integrated only on the bottom heated surface

where the wall temperature and the heat flux are the highest, in order to suppress liquid dry-out by generating capillary flow in the presence of menisci formation (Figure 1c). This capillary flow can be created both along the channel direction and from the sidewalls to the center (the dotted line regions in Figure 1a and 1b). The sidewalls have tailored roughness of 1-2 μm to promote nucleation [37]. By nucleating on the side walls, it is less likely to have dry-out occur on the bottom surface, which typically occurs in the case of smooth microchannel walls, owing to explosive bubble growth from it.

2.1 Device Design and Fabrication

We investigated single microchannels with typical characteristic dimensions of 10 mm in length, 500 μm in width, and 500 μm in height. We varied the micropillar geometries on the bottom surface of the microchannel with diameters of 5-10 μm, pitches of 10-40 μm, and constant heights of 25 μm. These micropillar geometries were chosen for the following reasons: (1) The micropillars are easy to fabricate in silicon (Si) using standard etching processes and the geometries can be well-controlled in this range. (2) At these length scales, the capillary pressures that can be generated are a few kPa which are comparable to the typical microchannel pressure drop. This suggests that capillary effects are not small and can be used to manipulate flow behavior. (3) The surface structures are mechanically robust and will not change morphology (deform or form clusters) as the liquid evaporates. The specific micropillar geometries fabricated and tested are shown in Table 1, which allows investigation of the effect of micropillar diameter d and pitch l on heat transfer and flow characteristics during flow boiling. Specifically, we aimed to maximize the liquid propagation coefficient in micropillar arrays with a fixed aspect ratio h/d but different pitches l based on a fluid wicking model developed by Xiao *et al.* [39].

To emulate the heat flux from a high performance electronic device, we integrated a thin-film metal heater (8.6 mm long × 380 μm wide) directly underneath the microchannel to serve as a heat source *via* Joule heating (Figure 1a and 2a). In addition to the heating element, we incorporated four thin-film resistance temperature detectors (RTDs), which are commonly used for flow boiling studies [22–24,40,41], along the length of the heater to measure the microchannel backside surface temperature at different locations. Specifically, the distances x of RTD1 through RTD4 from the inlet of the microchannel were 0 mm, 1.4 mm, 5.7 mm and 10 mm respectively (Figure 2a).

Standard silicon MEMS fabrication processes were used to create the microchannel test devices and are summarized in Figure 2. The micropillars were etched in a 500 μm thick Si wafer using deep reactive ion etching (DRIE) of the channel bottom surface (Figure 2b). A second 500 μm thick Si wafer was etched through using DRIE to define the channel sidewalls (Figure 2c). Inlet and outlet ports were created on a Pyrex wafer by laser drilling (Figure 2d). The two Si wafers were bonded together using direct Si-Si fusion bonding. A 1 μm silicon dioxide (SiO_2) layer was thermally grown on the Si surface as a hydrophilic coating on the channel walls and as an electrical insulation layer on the backside. The Pyrex wafer was subsequently bonded onto the Si wafers using anodic bonding to cover the microchannel and facilitate flow visualizations (Figure 2e). Finally, a layer of ~170 nm thick platinum (Pt) was deposited on the backside of the microchannel with electron-beam evaporation and patterned by lift-off technique to serve as the heater and RTDs (Figure 2f, 3b and 3c). To maximize the power dissipation capability of the heater, the target heater resistance was determined by the maximum allowable heater voltage (180 V) and current (0.5 A) to prevent burnout. To achieve this

target resistance of 360 Ω, we designed the thin film heater thickness and dimensions. In addition to the microstructured microchannels, we also fabricated microchannels with smooth surfaces following a similar procedure, however a polished Si wafer (roughness < 50 nm) was used instead of the micropillar wafer in the initial step (Figure 2b).

Figure 3a and 3b show the front and backside of a fabricated microchannel device. The two open chambers next to the microchannel (Figure 3a and 3d) were incorporated to minimize heat loss *via* conduction and to better isolate the effect of flow boiling in the microchannel. Figure 3c shows a magnified view of the Pt heater and an RTD on the backside of the microchannel. Figure 3d shows a scanning electron micrograph (SEM) of the cross-section of the microchannel (A-A plane in Figure 3a) with representative micropillars. The magnified views of micropillars on the channel bottom surface and a side wall near the bottom corner are shown in the left and right inset of Figure 3d. The side walls have small roughness (~1-2 μm) from the DRIE process (Figure 2c).

2.2 Experiment Methodology and Measurement Uncertainty

We developed a closed loop test rig to characterize the microchannel test devices during flow boiling (Figure 4). The loop consists of a liquid reservoir, a pump to provide a constant flow rate, a valve for flow stabilization, pre-heaters to minimize subcooling, a test fixture to interface with the test device, and various sensors. Degassed and high purity water (WX0004-1, OmniSolv) was used as the working fluid. Throughout the experiment, water in the liquid reservoir was heated and degassed to saturated conditions under atmospheric pressure ($T_{water,res}$ = 100 °C for $P_{water,res}$ = 1 atm). The fluid from the reservoir was pumped through the loop using a peristaltic pump (7528-30, Cole Parmer

MasterFlex L/S) to avoid contamination of the working fluid. In order to measure the flow rate with a liquid flow meter (L-50CCM-D, Alicat Scientific) which has a maximum working temperature of 60 °C, the degassed liquid was cooled *via* heat exchange with the ambient to below 60 °C as it passed through the metal tubing (the orange line in Figure 4 between the liquid reservoir and the flow meter). The mass flux chosen in this study was G = 300 kg/m^{2}s, which is a commonly used value in the literature [4,15–17]. In addition, this moderate mass flux allowed for high heat flux dissipation at reasonable pressure drops and pumping powers. To achieve this mass flux, the flow rate was maintained at 4.5 ml/min. We reduced the flow rate fluctuations intrinsic to the peristaltic pump by using a high pump speed (~70 rpm) with the smallest pump tubing available (tube ID = 0.8 mm, L/S 13, Masterflex) for the pump used in the study. However, flow rate fluctuations (± 0.6 ml/min) were inevitable with the peristaltic pump at these low mass fluxes. Accordingly, a metering valve (SS-SS4-VH, Swagelok) was used to create additional hydraulic resistance (~8 kPa) for flow stabilization within the loop, and was kept at a fixed opening for all the testing (the structured surface test samples and the smooth surface test sample). Since the liquid was subcooled due to heat loss to the ambient before the microchannel test section, we added pre-heaters (FGR-030, OMEGALUX) to compensate for this heat loss. The pre-heaters maintained a minimum liquid subcooling (10 °C) while also avoiding boiling at the entrance of the test fixture. Thermocouples (K type, Omega) and pressure transducers (PX319-030A5V, Omega) were used to monitor the loop conditions. The microchannel test devices were placed in an Ultem test fixture that interfaces with the loop. The test fixture was placed in an inverted microscope (TE2000-U, Nikon) and the flow was captured using a high speed

camera (Phantom v7.1, Vision Research) at 2000 frames/s. The two-phase flow pressure at the outlet of the microchannel was approximately P_{out} = 1 atm since it was connected to the liquid reservoir at atmospheric pressure.

Before the experiment, the Pt heater and RTDs were annealed at 400 °C for 1 hour to avoid resistance drift. The resistance R of the heater and RTDs after annealing was approximately 275 Ω at room temperature and 340 Ω at 120 °C. All the RTDs were calibrated in an oven and a linear correlation between the resistance and temperature was observed. The average sensitivity of the temperature with the resistance of the fabricated RTDs is $\Delta T = 1.4\Delta R$. The uncertainty of the resistance measurement (~1.4 Ω) resulted in an uncertainty of ±2 °C in the measured temperature. The microchannels were rinsed in acetone, isopropyl alcohol (IPA) and de-ionized water, and subsequently plasma cleaned in an oxygen environment (29 W at 500 mTorr for 15 minutes) to remove surface contamination. During the experiments, we heated the microchannel by applying a DC voltage across the thin-film heater. The microchannel heater was connected to a DC power supply (KLP 600-4-1200, Kepco), which was controlled using a PID algorithm in LabVIEW to maintain a constant output power. At each constant heat flux at steady state, the temperatures T_1 to T_4 measured by RTD1 to RTD4 respectively, the pressures and temperatures at the inlet and outlet of the microchannel, the flow rate, and the voltage and current across the heater were recorded for two minutes. The heat flux was then increased by an increment of approximately 20 W/cm^2 to the next value. Based on our measured temperature and pressure drop, the rise time to reach the next steady state was less than one minute due to the small thermal mass of the test device and the small temperature rise (~1-2 °C, see Appendix for details). In addition, we examined the measured steady state

temperature for ~5 min and no further rise was observed. Therefore the loop was left running for at least one minute to reach steady state before we acquired the data at this new heat flux. All the data was recorded using a data acquisition card (NI-PCI-6289, National Instruments) at a sample rate of 2 Hz. The experiments were performed twice for each sample under the same experimental conditions to verify repeatability (the samples were cleaned using the methods described here prior to each experiment). The experimental results were similar (within the error bars) and the data reported in this manuscript are from the repeated experiment. Since the microchannel is a three-layer stack that is bonded together, we cannot remove the cover layer (without damaging the sample) of the microchannel to measure the contact angle on the channel walls. However, wicking was observed with the structured surface microchannels before and after the experiment, which suggests an apparent contact angle of 0°.

The error bars in the experiments were estimated based on the uncertainty of the measurement from the instrument error ($error_{instrument}$) and the standard deviation (STD) of multiple data points for the time-averaged data, described by equation (1).

$$error = \sqrt{error_{instrument}^{\ 2} + STD^2} \tag{1}$$

The instrument error included the resolution of the pressure transducers (±300 Pa), the data acquisition card (±1 mV) which resulted in the uncertainty of the temperature measured by the RTDs (±2 °C), the power supply (0.06 V and 0.4 mA), and the flow meter (±1 ml/min).

2.3 Data Processing

Since the backside temperature (T_1 to T_4) varies along the microchannel (see Appendix for a representative measurement), we compared different samples using the

temperature values measured at the mid-point of the microchannel backside surface by RTD3 (T_3), where the highest heater surface temperatures were observed. The outlet temperature was lower than the center as expected due to heat spreading in the substrate. The temperature rise ΔT, obtained from the difference between the mid-point temperature and the saturation temperature of the fluid (T_{sat}) at this location, is

$$\Delta T = T_3 - T_{sat} \tag{2}$$

The fluid pressure and the corresponding saturation temperature (approximately 100 °C) also vary along the channel (see Appendix). The saturation pressure (P_{sat}) of the fluid at the mid-point location was determined as the average of the measured absolute pressure values at the inlet and outlet of the microchannel,

$$P_{sat} = \frac{1}{2}(P_{in} + P_{out}) \tag{3}$$

The mid-point saturation temperature was then obtained from the NIST database [42] using the calculated mid-point pressure P_{sat} (equation (3)). The heat flux was obtained from the input electrical power (DC voltage and current), the surface area of the channel bottom wall and accounting for the loss to the environment as,

$$q'' = \frac{0.95UI - P_{loss}}{A_{mc}} \tag{4}$$

where U is the input voltage, I is the input current, P_{loss} is the calibrated loss to the environment, A_{mc} is the microchannel bottom wall surface area (500 μm × 10 mm). The heat generated in the electrical connection lines to the contact pads (enclosed in the dotted line in Figure 2a) was 5% of the total heat from the power supply. The factor of 0.95 (5% loss) in equation (4) was obtained based on the geometry of this resistance relative to the total resistance using,

$$\frac{R_c}{R_{total}} = \frac{\frac{L_c}{W_c}}{\frac{L_c}{W_c} + \frac{L_{heater}}{W_{heater}}} = 0.05 \tag{5}$$

where R_c and R_{total} are the resistance of the connection lines and the total heater resistance, respectively, L_c, L_{heater}, W_c and W_{heater} are the length and width of the connection lines and the heater respectively. The temperature (at the heater surface) dependent heat loss to the environment P_{loss} measured by the RTDs was obtained from experiments where the test device in the fixture was heated with the flow loop evacuated (*i.e.*, no working fluid). A 2nd order polynomial (close to linear) fit (R^2 = 1) between P_{loss} (W) and the average microchannel backside surface temperature T_{ave} (°C) was determined from the experimental data as,

$$P_{loss} = 4.5 \times 10^{-5} T_{ave}^{\ 2} + 0.0163 T_{ave} - 0.299 \tag{6}$$

Since T_2, T_3 and T_4 are the backside surface temperatures at the inlet, mid-point and outlet of the microchannel respectively, if we approximate the first half of the microchannel backside surface temperature as $0.5(T_2+T_3)$, and the second half as $0.5(T_3+T_4)$, the average microchannel backside surface temperature can be approximated as,

$$T_{ave} = 0.25T_2 + 0.5T_3 + 0.25T_4 \tag{7}$$

The overall heat transfer coefficient (HTC) which includes boiling, evaporation and conduction through the bottom Si layer was calculated from the heat flux q'' and the time-averaged temperature rise ΔT as,

$$HTC = q'' / \Delta T \tag{8}$$

Due to the unstable nature of flow boiling, ΔT typically does not capture the dynamic behavior, such as periodic dry-out, which can also cause severe transient overheating issues. Therefore we defined CHF as the heat flux beyond which the

following criteria hold: (1) There is at least a 5 °C jump in ΔT; (2) There is constant or periodic dry-out in terms of time-resolved temperature and pressure drop measurements, and visualizations. In the case of periodic dry-out, the temperature fluctuations were larger than 20 °C, the pressure drop fluctuations were larger than 2 kPa, and the duration of dry-out was longer than half the cycle time.

3 RESULTS AND DISCUSSION

In this section, we first compare the stability of the measured temperature and pressure drop, and discuss the difference between the structured surface devices and the smooth surface device. Images and videos of the bottom heated surface were used to investigate the role of surface structures in annular flow stability. We then characterized the boiling curve and pressure drop curve, and discuss the heat transfer enhancement mechanism in the critical heat flux and heat transfer coefficient. Finally, we explain the different behavior among the structured surface microchannels by extension of a liquid wicking model and provide insights into the optimization of the micropillar geometries.

3.1 Temperature and Pressure Drop Fluctuations

Typically with smooth surface microchannels, flow instability can cause temperature and pressure drop fluctuations due to the change of flow pattern and local surface dry-out [43,44]. To study the effect of surface structures on flow instabilities, we measured the temporal change in the backside surface temperature and pressure drop across the microchannels with structured surfaces and compared to the fluctuations of a smooth surface microchannel. The mid-point backside surface temperature T_3 measured from RTD3 which was the highest temperature obtained compared to T_1, T_2 and T_4 was

studied for this purpose. The smooth surface and the structured surface microchannels showed similar and small fluctuations at low heat fluxes (q'' < 400 W/cm^2) for the mass flux investigated (G = 300 kg/m^{2}s), since the vapor quality was relatively low and dry-out of the thin liquid film was less likely to occur compared to that at higher heat fluxes. As the heat flux increased to q'' = 430 W/cm^2, temperature spikes and increased pressure drop fluctuations were observed for the smooth surface microchannels (Figure 5a). At the same heat flux, all the structured surface microchannels showed small temperature (±5 °C) and pressure drop fluctuations (±300 Pa), and the data of one representative structured surface device (S4) is shown in Figure 5a. From the visualization of the flow (Supplementary Video and Figure 5a), the temperature spikes of the smooth surface correspond to dry-out at the bottom microchannel surface. In contrast, flow visualization of the structured surface microchannel (Figure 5a and Supplementary Video) indicated a stable liquid film covering the microchannel bottom surface. This stable liquid film contributed to the stability of the temperature and the pressure drop significantly. Dry-out on the structured surface occurred less frequently with shorter durations and less dry surface area compared to the smooth surface (Supplementary Video).

With further increases in heat flux, the temperature spikes observed on the smooth surface microchannel occurred more often and gradually developed to large amplitude (>20 °C) periodic dry-out (Figure 5b and 5c at q'' = 520 W/cm^2 and 615 W/cm^2 respectively). In comparison, the structured surface microchannel showed stable temperature (±5 °C) and pressure drop (±300 Pa) at the same heat flux (Figure 5b to 5c), even at CHF (±5-7 °C and ±300-600 Pa, Figure 6).

To further investigate the role of the structures during the dry-out process, we compared visualizations of the flow on a smooth surface and on a representative structured surface (Figure 7, q'' = 430 W/cm^2, G = 300 kg/m^{2}s). At t = 0 s both microchannels were in the annular flow regime. At t > 0 s, the annular liquid volume started to reduce. Dry-out occurred first from the corners on the smooth surface (t = 0.002 s), and the dry surface area expanded to the center of the microchannel (0.002 s<t<0.010 s), leaving individual liquid islands. Due to the inability to supply liquid to the surface, the smooth surface could not maintain this liquid film and thus the dry-out area expanded. The smooth surface was completely dry from t = 0.012 s to 0.022 s before the liquid built up at the inlet re-flushed the channel at t = 0.024 s.

In comparison, the structured surface (S4) maintained the liquid film due to the wicking capability of the microstructures (0.002 s<t<0.010 s), until vapor/dry islands formed first at the center instead of the sides of the channel from t=0.012 s (Figure 7). This suggests that there is wicking from the sides to the center where the propagation distance is the longest. This wicking sustained the liquid film (0.002 s<t<0.010 s) and delayed dry-out (t>0.012 s). In general, the wicking from the structures prevented dry-out from occurring (Supplementary Video). In addition, the dry patches formed at downstream locations before the upstream locations, which indicate that there is also wicking along the microchannel length. From the above observations, it is evident capillarity generated with the structures plays a significant role in stabilizing the liquid thin film and the resulting surface temperature.

3.2 Heat Transfer Performance Characterization

We also characterized the time-averaged heat transfer performance of the structured surface microchannels. We compared the heat flux q'' calculated by equation (4) as a function of the time-averaged mid-point backside surface temperature rise ΔT (equation (2)) for the four microstructured surface devices (Table 1) and the smooth surface device investigated, as shown in Figure 8a (*i.e.*, the boiling curves). The y-axis intercept (~50 W/cm^2) at ΔT = 0 °C was mainly due to the 10 °C subcooling, which agrees well with the estimated heat flux due to subcooling $q''_{subcooling} = \dot{m}c_p\Delta T_{subcooling}/A_{mc}$ = 63 W/cm^2. The low-slope in the curves at q'' below 150 W/cm^2 was due to single phase heat transfer where the onset of nucleate boiling was indicated by the sudden drop in ΔT. After the onset of nucleate boiling, the temperature rise increased with the heat flux.

The red arrows in the boiling curves (Figure 8a) indicate the CHF. The structured surface microchannels had a clear transition at CHF, which can be seen by the sudden drop in the boiling curve slope after CHF. The time-resolved temperature and pressure drop were also very stable before and at CHF (Figure 6). In contrast, the smooth surface microchannel had a less obvious transition to CHF, since periodic dry-out occurred much earlier on the boiling curve from q'' = 430 W/cm^2, as indicated by the temperature spikes (Figure 5). The large error bars of ΔT for the smooth surface devices at high heat fluxes were also due to the increasing temperature oscillations (Figure 8a). This resulted in a higher time averaged temperature rise under the same heat flux compared with the structured surface microchannels and thus a gradual decrease in the boiling curve slope. As the heat flux increased, flow instabilities (temperature spikes and pressure drop

oscillations) developed to large amplitude periodic dry-out or constant dry-out (longer than one minute).

The structured surface showed an enhanced CHF with a maximum value of 969 W/cm^2 at a corresponding vapor quality χ of 0.29 achieved by device S4, which is a 57% enhancement compared with that of the smooth surface microchannel (615 W/cm^2 at χ = 0.19). This CHF value is significant in comparison with similar studies in literature for a mass flux G of 300 kg/m^{2}s. The corresponding heat transfer coefficients (HTC) which were obtained from Figure 8a and equation (8) are shown in Figure 8b. The structured surface microchannels showed significantly enhanced HTC even at heat fluxes close to CHF. This is due to the fact that evaporation is dominant in the annular flow, and the structures facilitate a stable liquid film and the menisci increased the thin film area. The HTC of the structured surface devices were relatively constant, which indicates that dry-out was minimized by the structures and the thermal resistance remained relatively unchanged.

3.3 Pressure Drop

The hydrodynamic characteristics of the microchannels were also studied since pumping cost penalties can limit implementation of the solution in flow boiling systems [4]. Figure 9 shows the measured time-averaged pressure drop as a function of heat flux q''. The pressure drops across all devices were similar, which indicates that the additional pressure drop introduced by the surface structures in this study were negligible. The maximum ΔP was 14.3 kPa for device S4 at q'' = 969 W/cm^2 and G = 300 kg/m^{2}s, which resulted in a negligible pumping power of $P_{pump} = Q\Delta P$ = 1 mW, where Q is the

volumetric flow rate (m^3/s). This implies that the structures did not cost more pumping power while they maintained the temperature stability and enhanced heat transfer. This result is attributed to the liquid-vapor interface only forming menisci within the structures when there is insufficient liquid supply (Figure 1c) which is usually at the downstream section of the microchannel. In the devices tested, there was sufficient liquid supply upstream such that the majority of liquid was on top of the structures and the structures only acted as surface roughness and did not introduce noticeable extra viscous pressure drop. In addition, wicking from the sidewalls to the center of the bottom surface as discussed in Section 3.1 did not contribute to the pressure drop along the microchannel direction.

3.4 Wicking Model

To further support our explanation for the role of the micropillar geometries in the wicking performance, we predicted the transverse liquid propagation flow rate (from the side walls to the center) in the micropillar arrays (Figure 1c) using an adiabatic (no phase-change) wicking model developed by Xiao *et al.* [39]. The model solves the 1-D Brinkman equation to obtain the liquid velocity in porous media. Details of the model framework are listed in the Appendix, which gives the velocity profile,

$$u = Ae^{\alpha\sqrt{\varepsilon}y} + Be^{\alpha\sqrt{\varepsilon}y} - \frac{1}{\alpha^2\mu}\frac{dP}{dx} \tag{9}$$

where u is the velocity, dP/dx is the pressure gradient which drives the liquid flow, μ is the viscosity of the liquid, ε is the porosity of the micropillar arrays, and α^{-2} is the permeability that accounts for the drag introduced by porous media, A and B are constants listed in Appendix.

To estimate the driving pressure gradient dP/dx in equation (9) in the transverse direction of the microchannel, we assume that (1) the dry-out location has the largest meniscus curvature k (*i.e.*, minimum radius of curvature $r = 1/k$, Figure 1c) since the liquid level is the lowest. Therefore the liquid pressure is the lowest at the dry-out point based on the Young-Laplace equation ($P_{cap} = P_{vapor} - P_{liquid} = 2\sigma/r$); (2) at the dry-out location, the contact angle of water on silicon dioxide (pillar surface) is the receding contact angle θ_r ($\theta_r \approx 15^o$) [45]; (3) the pressure gradient is approximated as $dP/dx = (P_{max} - P_{min})/L_w$, where P_{max} is the maximum pressure along the wicking path which is at the sidewalls ($P_{max} \approx P_{vapor}$) since the curvature is approximately zero, $P_{\min}$ is the pressure at the dry-out location ($P_{min} = P_{vapor} - 2\sigma/r$), and L_w is the wicking distance. From above, $dP/dx = P_{cap}/L_w$; (4) P_{cap} is derived using a force balance on the liquid-vapor interface, $P_{cap}(l^2 - 0.25\pi d^2) = \gamma \pi d \cos\theta_r$ [46,47]; (5) the longest wicking distance is from one sidewall to the other sidewall since dry-out can happen at random locations, so maximum $L_w = W$, where W is the width of the microchannel ($W = 500$ μm). With these assumptions, we calculated the average liquid wicking velocity u_{ave} which is proportional to the flow rate of the wicking liquid film,

$$u_{ave} = \frac{1}{h}\int_{y=0}^{y=h} u dy \tag{10}$$

where the height h is fixed ($h = 25$ μm). The result is shown in Figure 10, where u_{ave} is plotted as a function of l and d. The geometries of the micropillars investigated in this study are also shown in symbols in Figure 10 (device S1 to S4).

By comparing the results in Figure 10 and Figure 8a, the microstructures that led to a higher liquid wicking velocity also had a higher CHF. This positive correlation between wicking velocity and CHF is expected based on our proposed mechanism, since

efficient liquid transport helped sustain the thin film evaporation and prevent dry-out. Figure 10 also indicates that the wicking velocity depends both on the capillary pressure which creates the driving pressure gradient, and the viscous resistance, which hinders effective liquid propagation. Both terms depend on the structure geometry. Specifically, the capillary pressure approximately scales with $1/l$, and the viscous drag scales with $1/l^2$, thus as l decreases the drag force increases faster than the driving capillary pressure. This is the reason device S1 has lower wicking velocity even though it has higher capillary pressure (due to smaller spacing) compared to device S4, because the increased viscous resistance is more significant than the increase of the pressure gradient. In fact, the geometry of the structures can be further optimized to maximize the wicking capability, and hence enhance the flow stability and heat transfer.

While this wicking model explains the trends of our results, there are limitations. First, the effects of evaporation and the curved interfaces were not accounted for. A more detailed numerical model which takes these two factors into consideration can be found in [46]. In addition, this model cannot predict the liquid velocity along the channel direction due to the existence of vapor shear stress (*i.e.*, an axially varying vapor pressure). This axial direction velocity is also important in determining the CHF in microchannels. A more comprehensive model which accounts for evaporation and wicking in both lateral and axial direction needs to be developed in the future to provide more detailed understanding of the role of surface structures on flow boiling.

4 CONCLUSIONS

We have demonstrated the design of a two-phase microchannel heat sink incorporated with micropillar arrays as a platform to study the effect of surface structures on flow boiling in microchannels. The design decouples thin film evaporation and nucleation by promoting capillary flow on the bottom heated surface while facilitating nucleation from the sidewalls. The structures reduced flow boiling instability significantly in the annular flow regime, and achieved very stable surface temperature and channel pressure drop even at high heat fluxes close to CHF. The smooth surface showed frequent temperature spikes and pressure drop fluctuations due to dry-out, which developed gradually to CHF. Visualization of the flow pattern and the dry-out process indicates that the micropillar surface can promote capillary flow and increase flow stability by maintaining a stable annular flow and high-performance thin film evaporation. This stabilized annular flow and thin film evaporation contributed to an enhanced HTC and CHF (maximum 57%) compared to a smooth surface microchannel. The pressure drop across all devices was similar, which indicates that the additional pressure drop introduced by the surface structures in this study was negligible. A liquid wicking model in the transverse direction of the channel was developed to explain the trend in the enhancement of CHF among the structured devices. Both the experimental results and the model suggest that capillary pressure can be maximized without introducing large viscous resistance when the microstructure geometry is optimized. A more comprehensive model that accounts for wicking in the microchannel axial direction will be developed in the future to aid in further understanding of the role of surface structures on flow boiling. This work provides important insights into the role and

promise of incorporating micropillar designs in high performance microchannel heat sinks.

ACKNOWLEDGMENT

This work was partially funded by the Office of Naval Research (ONR) with Dr. Mark Spector as program manager (N00014-15-1-2483), the Cooperative Agreement between the Masdar Institute of Science and Technology (Masdar Institute), Abu Dhabi, UAE and the Massachusetts Institute of Technology (MIT), Cambridge, MA, USA - Reference 02/MI/MI/CP/11/07633/GEN/G/00, the Battelle Memorial Institute, the Air Force Office of Scientific Research (AFOSR) and the Singapore-MIT Alliance for Research and Technology (SMART). The research was technically supported and encouraged by the Jet Propulsion Laboratory, California Institute of Technology, under a contract with the National Aeronautics and Space Administration. The authors would also like to acknowledge the MIT Microsystems Technology Lab for fabrication staff support, help, and use of equipment.

NOMENCLATURE

A_{mc} = microchannel bottom wall surface area
c_p = specific heat of water
d = diameter of the micropillar
G = mass flux in the microchannel
h = height of the micropillar
I = input current from the power supply
k = curvature of the meniscus
L_c = length of the electrical connection resistance
L_{heater} = length of the heater resistance

L_w = wicking distance

l = pitch of the micropillar

$\dot{m}$ = mass flow rate

ΔP = pressure drop across the microchannel

P_{cap} = capillary pressure

P_{in} = microchannel inlet pressure

P_{liquid} = liquid pressure

P_{loss} = calibrated heat loss to the environment

P_{out} = microchannel outlet pressure

P_{pump} = pumping power

P_{sat} = saturation pressure

P_{vapor} = vapor pressure

$P_{water,res}$ = pressure of the water in the reservoir

Q = volumetric flow rate

q'' = heat flux

$q''_{subcooling}$ = heat flux due to subcooling

ΔR = electrical resistance change

R = electrical resistance

R^2 = coefficient of determination

R_c = electrical connection resistance

R_{total} = total heater resistance

r = radius of curvature

ΔT = temperature rise/temperature change

$\Delta T_{subcooling}$ = subcooling

T_1 = temperature measured by RTD1

T_2 = temperature measured by RTD2

T_3 = temperature measured by RTD3

T_4 = temperature measured by RTD4

T_{ave} = average microchannel backside surface temperature

T_{sat} = saturation temperature

$T_{water,res}$ = temperature of the water in the reservoir

U = input voltage from the power supply

u = velocity

u_{ave} = average velocity

W = width of the microchannel

W_c = width of the electrical connection resistance

W_{heater} = width of the heater resistance

x = distance to the inlet of the microchannel

α^{-2} = permeability

ε = porosity of micropillar arrays

θ_r = receding contact angle

μ = viscosity

σ = surface tension

χ = vapor quality

Appendix

Time Required to Reach Steady State

We determined that the time of at least 1 minute was needed to reach the steady state as the heat flux was incremented by ~20 W/cm^2. This was based on our experimental observation where we constantly monitored the device temperature and pressure. A typical temperature response as the heat flux was incremented is shown in Figure A1 (Sample S2). We measured the steady state temperature for ~5 minutes and the average temperature was constant (no further rise was observed). This fast response is due to the small thermal mass of our device (1 mm thick silicon of 1 cm×3 cm area) and a small temperature rise of ~1-2 °C (shown in the boiling curve, Figure 8) associated with a small increment of heat flux (~20 W/cm^2). In addition, our flow loop was optimized to have minimal influence on the rise time of the microchannel: the inlet water temperature and

flow rate were kept constant, and the flow exiting the microchannel directly entered the constant pressure water reservoir (~1 L, 1 atm).

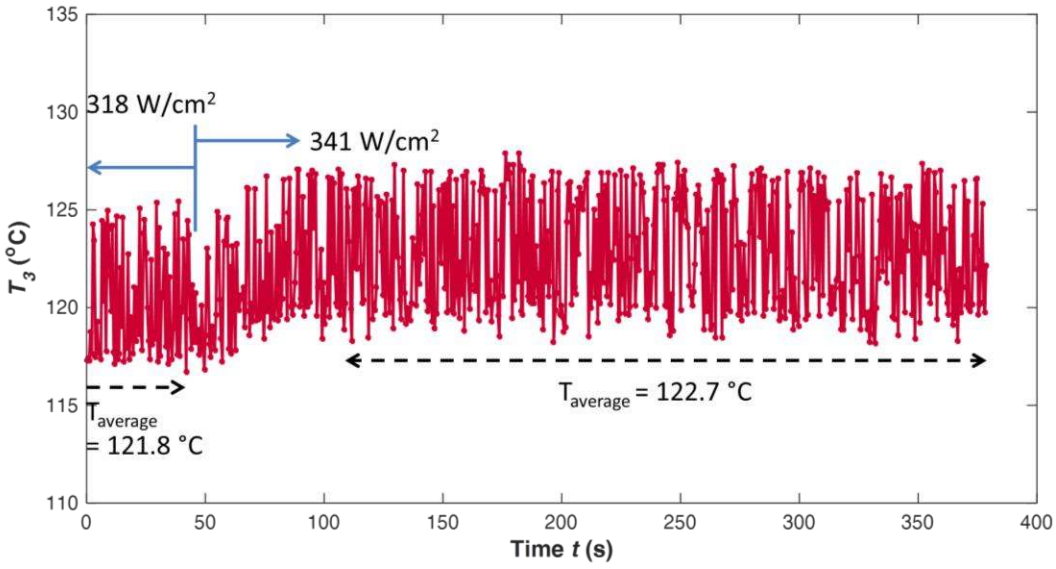

Figure A1. Mid-point microchannel backside temperature T_3 for sample S2. At t=45 s the heat flux was increased to 341 W/cm^2.

Temperature and Pressure Variation along the Microchannel

Figure A2a shows the measured backside temperature at the inlet (T_1, T_2), the mid-point (T_3) and the outlet (T_4) of the microchannel (Sample S4, q= 618 W/cm^2). The inlet temperature was close to the saturation temperature, and the mid-point temperature was the highest among the four measured temperatures. The outlet temperature was lower than the mid-point temperature. Figure A2b shows the inlet and outlet pressure, and the corresponding fluid saturation temperature. Since the device did not have temperature sensors on the microchannel inner wall surface, we were not able to measure the temperature at the channel wall (the solid-water interface). We did not estimate the wall

temperature based on the backside temperature due to complex heat spreading in the substrate to the channel bottom surface and to the side walls of the microchannel.

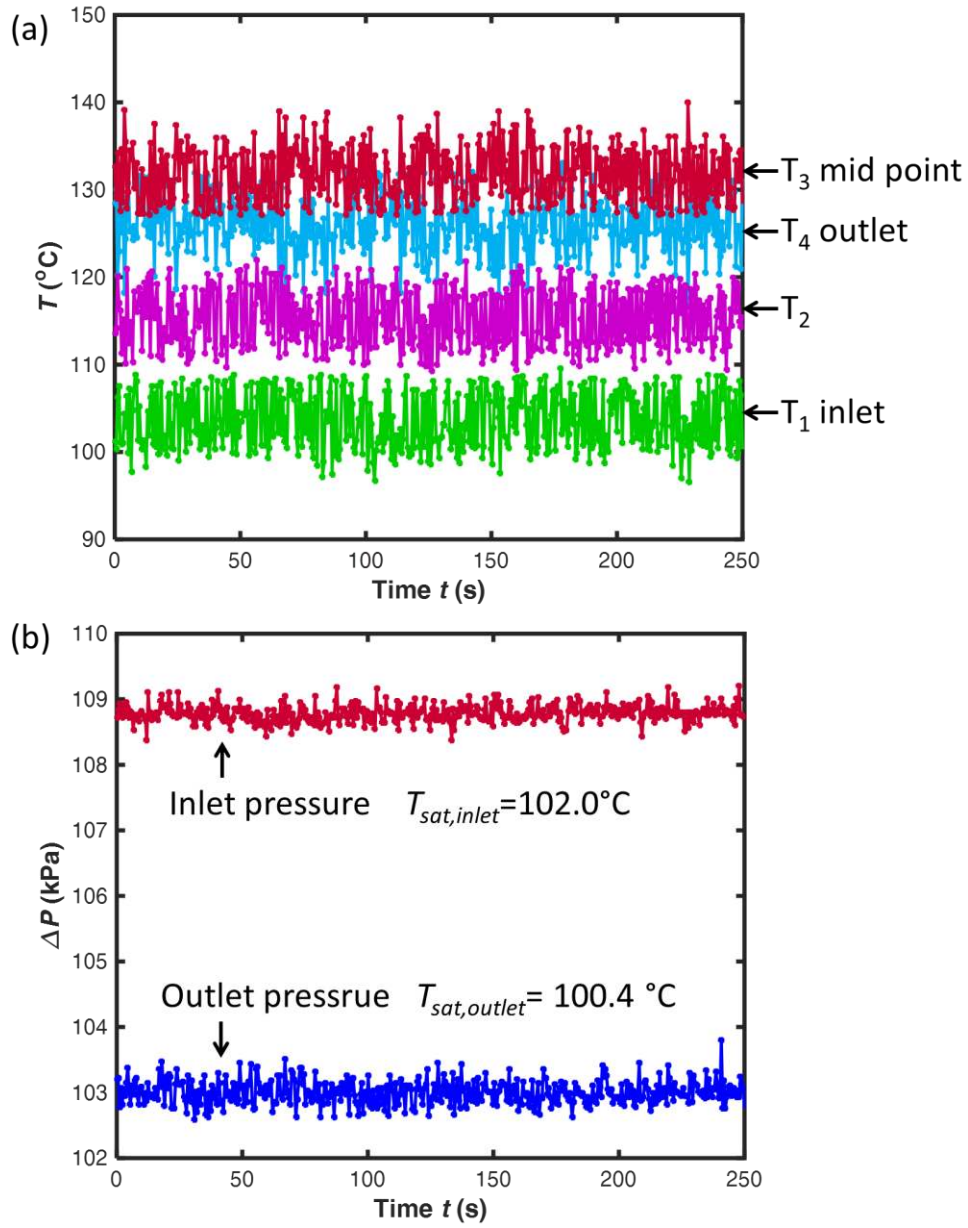

Figure A2. (a) Measured backside temperature at the inlet (T_1, T_2), the mid-point (T_3) and the outlet (T_4) of the microchannel (Sample S4, q= 618 W/cm^2). (b) The inlet and outlet pressure, and the corresponding fluid saturation temperature.

Wicking Model

The model by Xiao *et al*. [39] minimizes surface energy to predict the equilibrium liquid-vapor interface meniscus shape and thus the capillary pressure generated by the pillar arrays. The liquid velocity profile was analytically solved using the one-dimensional form of the Brinkman equation [48] as shown in equation (A1), which is a modified form of the Navier-Stokes equation including a Darcy term to study flow through porous media.

$$\mu \frac{d^2u}{dy^2} - \varepsilon \frac{dP}{dx} - \mu\alpha^2 \varepsilon u = 0 \tag{A1}$$

In equation (A1), u is the velocity, dP/dx is the pressure gradient which drives the liquid flow, μ is the viscosity of the liquid, ε is the porosity of the micropillar arrays, and α^{-2} is the permeability that accounts for the drag introduced by porous media. The micropillars were regarded as porous media with permeability numerically studied by Sangani and Acrivos [49], and the expression is given by,

$$a^{-2} = l^2 \frac{\ln c^{-1/2} - 0.738 + c - 0.887c^2 + 2.038c^3 + O(c^4)}{4\pi} \tag{A2}$$

where $c = \pi d^2/4l^2$ is the solid fraction. We assume no slip boundary condition (u = 0) at y = 0 (bottom surface) and a shear free boundary condition at the pillar tops (du/dy = 0 at $y = h$ = 25 μm, where h is the height of the pillars). Since we only model the wicking process in the cross sectional plane (from the sidewalls inwards), it is reasonable to neglect shear at $y = h$ in the lateral direction, since the shear force is mainly along the channel direction due to the vapor flow.

With the boundary conditions, the velocity field is expressed as equation (9) [39], where the constants A and B in equation (9) are,

$$A = \frac{dP/dx \exp(-\alpha h\sqrt{\varepsilon})}{\alpha^2 \mu[\exp(\alpha h\sqrt{\varepsilon}) + \exp(-\alpha h\sqrt{\varepsilon})]} \tag{A3}$$

$$B = \frac{dP/dx \exp(\alpha h\sqrt{\varepsilon})}{\alpha^2 \mu[\exp(\alpha h\sqrt{\varepsilon}) + \exp(-\alpha h\sqrt{\varepsilon})]} \tag{A4}$$

REFERENCES

[1] Pop, E., 2010, "Energy dissipation and transport in nanoscale devices," Nano Res., **3**(3), pp. 147–169.

[2] Thome, J. R., 2006, "The New Frontier in Heat Transfer: Microscale and Nanoscale Technologies," Heat Transf. Eng., **27**(9), pp. 1–3.

[3] Krishnan, S., Garimella, S. V., Chrysler, G. M., and Mahajan, R. V., 2007, "Towards a Thermal Moore's Law," IEEE Trans. Adv. Packag., **30**(3), pp. 462–474.

[4] Kandlikar, S. G., 2002, "Fundamental issues related to flow boiling in minichannels and microchannels," Exp. Therm. Fluid Sci., **26**(2–4), pp. 389–407.

[5] Das, P. K., Chakraborty, S., and Bhaduri, S., 2012, "Critical Heat Flux During Flow Boiling in Mini And Microchannel-A State of The Art Review," Front. Heat Mass Transf., **3**(1).

[6] Bergles, A. E., V, J. H. L., Kendall, G. E., and Griffith, P., 2003, "Boiling and Evaporation in Small Diameter Channels," Heat Transf. Eng., **24**(1), pp. 18–40.

[7] Hetsroni, G., Mosyak, A., Pogrebnyak, E., and Segal, Z., 2005, "Explosive boiling of water in parallel micro-channels," Int. J. Multiph. Flow, **31**(4), pp. 371–392.

[8] Zhang, T., Peles, Y., Wen, J. T., Tong, T., Chang, J.-Y., Prasher, R., and Jensen, M. K., 2010, "Analysis and active control of pressure-drop flow instabilities in boiling microchannel systems," Int. J. Heat Mass Transf., **53**(11–12), pp. 2347–2360.

[9] Zhang, T., Tong, T., Chang, J.-Y., Peles, Y., Prasher, R., Jensen, M. K., Wen, J. T., and Phelan, P., 2009, "Ledinegg instability in microchannels," Int. J. Heat Mass Transf., **52**(25–26), pp. 5661–5674.

[10] Yadigaroglu, G., and Bergles, A. E., 1972, "Fundamental and Higher-Mode Density-Wave Oscillations in Two-Phase Flow," J. Heat Transf., **94**(2), pp. 189–195.

[11] Bergles, A. E., and Kandlikar, S. G., 2005, "On the Nature of Critical Heat Flux in Microchannels," J. Heat Transf., **127**(1), pp. 101–107.

[12] Koşar, A., Kuo, C.-J., and Peles, Y., 2005, "Suppression of Boiling Flow Oscillations in Parallel Microchannels by Inlet Restrictors," J. Heat Transf., **128**(3), pp. 251–260.

[13] Wang, G., Cheng, P., and Bergles, A. E., 2008, "Effects of inlet/outlet configurations on flow boiling instability in parallel microchannels," Int. J. Heat Mass Transf., **51**(9–10), pp. 2267–2281.

[14] Kandlikar, S. G., Kuan, W. K., Willistein, D. A., and Borrelli, J., 2005, "Stabilization of Flow Boiling in Microchannels Using Pressure Drop Elements and Fabricated Nucleation Sites," J. Heat Transf., **128**(4), pp. 389–396.

[15] Koşar, A., Kuo, C.-J., and Peles, Y., 2005, "Boiling heat transfer in rectangular microchannels with reentrant cavities," Int. J. Heat Mass Transf., **48**(23–24), pp. 4867–4886.

[16] David, M. P., Steinbrenner, J. E., Miler, J., and Goodson, K. E., 2011, "Adiabatic and diabatic two-phase venting flow in a microchannel," Int. J. Multiph. Flow, **37**(9), pp. 1135–1146.

[17] Alexander, B. R., and Wang, E. N., 2009, "Design of a Microbreather for Two-Phase Microchannel Heat Sinks," Nanoscale Microscale Thermophys. Eng., **13**(3), pp. 151–164.
[18] Fazeli, A., Mortazavi, M., and Moghaddam, S., 2015, "Hierarchical biphilic micro/nanostructures for a new generation phase-change heat sink," Appl. Therm. Eng., **78**, pp. 380–386.
[19] Koşar, A., and Peles, Y., 2007, "Boiling heat transfer in a hydrofoil-based micro pin fin heat sink," Int. J. Heat Mass Transf., **50**(5–6), pp. 1018–1034.
[20] Wang, Y., and Peles, Y., 2015, "Subcooled flow boiling in a microchannel with a pin fin and a liquid jet in crossflow," Int. J. Heat Mass Transf., **86**, pp. 165–173.
[21] Woodcock, C., Yu, X., Plawsky, J., and Peles, Y., 2015, "Piranha Pin Fin (PPF) — Advanced flow boiling microstructures with low surface tension dielectric fluids," Int. J. Heat Mass Transf., **90**, pp. 591–604.
[22] Li, D., Wu, G. S., Wang, W., Wang, Y. D., Liu, D., Zhang, D. C., Chen, Y. F., Peterson, G. P., and Yang, R., 2012, "Enhancing Flow Boiling Heat Transfer in Microchannels for Thermal Management with Monolithically-Integrated Silicon Nanowires," Nano Lett., **12**(7), pp. 3385–3390.
[23] Yang, F., Dai, X., Peles, Y., Cheng, P., Khan, J., and Li, C., 2014, "Flow boiling phenomena in a single annular flow regime in microchannels (I): Characterization of flow boiling heat transfer," Int. J. Heat Mass Transf., **68**, pp. 703–715.
[24] Yang, F., Dai, X., Peles, Y., Cheng, P., Khan, J., and Li, C., 2014, "Flow boiling phenomena in a single annular flow regime in microchannels (II): Reduced pressure drop and enhanced critical heat flux," Int. J. Heat Mass Transf., **68**, pp. 716–724.
[25] Dhir, V. K., 1998, "Boiling Heat Transfer," Annu. Rev. Fluid Mech., **30**(1), pp. 365–401.
[26] Chen, R., Lu, M.-C., Srinivasan, V., Wang, Z., Cho, H. H., and Majumdar, A., 2009, "Nanowires for Enhanced Boiling Heat Transfer," Nano Lett., **9**(2), pp. 548–553.
[27] Li, C., Wang, Z., Wang, P.-I., Peles, Y., Koratkar, N., and Peterson, G. P., 2008, "Nanostructured Copper Interfaces for Enhanced Boiling," Small, **4**(8), pp. 1084–1088.
[28] Ahn, H. S., Jo, H. J., Kang, S. H., and Kim, M. H., 2011, "Effect of liquid spreading due to nano/microstructures on the critical heat flux during pool boiling," Appl. Phys. Lett., **98**(7), p. 071908.
[29] Rahman, M. M., Ölçeroğlu, E., and McCarthy, M., 2014, "Role of Wickability on the Critical Heat Flux of Structured Superhydrophilic Surfaces," Langmuir, **30**(37), pp. 11225–11234.
[30] Chu, K.-H., Enright, R., and Wang, E. N., 2012, "Structured surfaces for enhanced pool boiling heat transfer," Appl. Phys. Lett., **100**(24), p. 241603.
[31] Chu, K.-H., Soo Joung, Y., Enright, R., Buie, C. R., and Wang, E. N., 2013, "Hierarchically structured surfaces for boiling critical heat flux enhancement," Appl. Phys. Lett., **102**(15), pp. 151602–151602–4.
[32] Betz, A. R., Jenkins, J., Kim, C.-J. "CJ," and Attinger, D., 2013, "Boiling heat transfer on superhydrophilic, superhydrophobic, and superbiphilic surfaces," Int. J. Heat Mass Transf., **57**(2), pp. 733–741.
[33] Betz, A. R., Xu, J., Qiu, H., and Attinger, D., 2010, "Do surfaces with mixed hydrophilic and hydrophobic areas enhance pool boiling?," Appl. Phys. Lett., **97**(14), p. 141909.

[34] Shin, S., Choi, G., Kim, B. S., and Cho, H. H., 2014, "Flow boiling heat transfer on nanowire-coated surfaces with highly wetting liquid," Energy, **76**, pp. 428–435.
[35] Kleinstreuer, C., and Koo, J., 2004, "Computational Analysis of Wall Roughness Effects for Liquid Flow in Micro-Conduits," J. Fluids Eng., **126**(1), pp. 1–9.
[36] Bahrami, M., Yovanovich, M. M., and Culham, J. R., 2005, "Pressure Drop of Fully Developed, Laminar Flow in Rough Microtubes," J. Fluids Eng., **128**(3), pp. 632–637.
[37] Hsu, Y. Y., 1962, "On the Size Range of Active Nucleation Cavities on a Heating Surface," J. Heat Transf., **84**(3), pp. 207–213.
[38] Carey, V. P., 2007, Liquid Vapor Phase Change Phenomena: An Introduction to the Thermophysics of Vaporization and Condensation Processes in Heat Transfer Equipment, Second Edition, Taylor & Francis.
[39] Xiao, R., Enright, R., and Wang, E. N., 2010, "Prediction and Optimization of Liquid Propagation in Micropillar Arrays," Langmuir, **26**(19), pp. 15070–15075.
[40] Rao, S. R., and Peles, Y., 2015, "Spatiotemporally resolved heat transfer measurements for flow boiling in microchannels," Int. J. Heat Mass Transf., **89**, pp. 482–493.
[41] Rao, S. R., Houshmand, F., and Peles, Y., 2014, "Transient flow boiling heat-transfer measurements in microdomains," Int. J. Heat Mass Transf., **76**, pp. 317–329.
[42] Lemmon, E. W., Huber, M. L., and McLinden, M. O., 2013, NIST Standard Reference Database 23, National Institute of Standards and Technology.
[43] Kuo, C.-J., and Peles, Y., 2008, "Flow Boiling Instabilities in Microchannels and Means for Mitigation by Reentrant Cavities," J. Heat Transf., **130**(7), pp. 072402–072402.
[44] Wu, H. Y., and Cheng, P., 2003, "Visualization and measurements of periodic boiling in silicon microchannels," Int. J. Heat Mass Transf., **46**(14), pp. 2603–2614.
[45] Raj, R., Maroo, S. C., and Wang, E. N., 2013, "Wettability of Graphene," Nano Lett., **13**(4), pp. 1509–1515.
[46] Zhu, Y., Antao, D. S., Lu, Z., Somasundaram, S., Zhang, T., and Wang, E. N., 2016, "Prediction and Characterization of Dry-out Heat Flux in Micropillar Wick Structures," Langmuir. DOI: 10.1021/acs.langmuir.5b04502
[47] Antao, D. S., Adera, S., Zhu, Y., Farias, E., Raj, R., and Wang, E. N., 2016, "Dynamic Evolution of the Evaporating Liquid–Vapor Interface in Micropillar Arrays," Langmuir, **32**(2), pp. 519–526.
[48] Brinkman, H. C., 1949, "A calculation of the viscous force exerted by a flowing fluid on a dense swarm of particles," Appl. Sci. Res., **1**(1), pp. 27–34.
[49] Sangani, A. S., and Acrivos, A., 1982, "Slow flow past periodic arrays of cylinders with application to heat transfer," Int. J. Multiph. Flow, **8**(3), pp. 193–206.

Figure Captions List

Fig. 1 Schematic of the microchannel heat sink design with micropillars on the heated surface. (a) Side view, (b) cross-section view, and (c) magnified view of the liquid film forming menisci which create the capillary pressure gradient, dP/dx, that helps drive the liquid flow. The equation that describes the liquid pressure below the meniscus is the Young-Laplace equation where σ is the surface tension of the liquid, r is the radius of curvature of the local meniscus, and P_{liquid} and P_{vapor} are the local pressure of the liquid and vapor respectively.

Fig. 2 Design and fabrication process of the microchannel device. (a) Schematic (to scale) of the heater and RTDs on the backside of the microchannel device. The dotted sections are the electrical connection lines to the contact pads. (b) Micropillars of 25 μm height were etched in Si using deep reactive ion etching (DRIE). (c) A Si wafer was etched through using DRIE to define the channel. (d) Inlet and outlet ports were laser-drilled on a Pyrex glass wafer. (e) The Si layers were bonded using direct Si-Si bonding. A silicon dioxide (SiO_2) layer was thermally grown on the Si surface. The Pyrex layer was bonded to the top Si layer using anodic bonding. (f) A platinum (Pt) layer was deposited on the backside of the microchannel using electron-beam evaporation and patterned to form the heater and RTDs.

Fig. 3 Images of a representative fabricated microchannel with micropillar

arrays. Optical images of the (a) front and (b) backside of a device. (c) Optical microscope image of the heater and RTD4 on the backside of the microchannel. (d) SEM image of the cross section (A-A plane in 3a) of a microchannel with magnified view of the micropillars (left inset) and a sidewall at the bottom corner (right inset).

Fig. 4 Schematic of the custom flow boiling loop used in the study. The loop consists of a liquid reservoir, a pump to provide a constant flow rate, a valve for flow stabilization, pre-heaters to minimize subcooling, a test fixture to interface with the test device, and various sensors. The components "P", "T" and "M" indicate locations of pressure transducers, thermocouples and the liquid flow meter respectively.

Fig. 5 Temporally resolved temperature and pressure drop, and flow visualization at G = 300 kg/m^{2}s. (a) Mid-point backside surface temperature T_3 and pressure drop across a smooth surface microchannel and a structured surface microchannel S4 at q'' = 430 W/cm^2. Insets are optical images of a smooth bottom channel surface and a structured bottom channel surface (S4). Mid-point backside surface temperature T_3 and pressure drop of a smooth surface microchannel and a structured surface microchannel S4 at (b) q'' = 520 W/cm^2 and (c) q'' = 615 W/cm^2. The uncertainties of the temperature and pressure drop measurement were approximately ±2 °C and ±300 Pa.

Fig. 6 Mid-point backside surface temperature T_3 and pressure drop ΔP fluctuations of the structured surface microchannels at CHF (the highest

heat flux beyond which dry-out occurred). (a) device S1 at q'' = 655 W/cm^2, (b) device S2 at q'' = 763 W/cm^2, (c) device S3 at q'' = 819 W/cm^2 and (d) device S4 at q'' = 969 W/cm^2. The mass flux G = 300 kg/m^{2}s. The uncertainties of the temperature and pressure drop measurement were approximately ±2 °C and ±300 Pa.

Fig. 7 Time-lapse images of the dynamic dry-out process on a smooth surface and on a structured surface (S4) captured by a high speed camera. q'' = 430 W/cm^2 and G = 300 kg/m^{2}s. The structured surface showed less dry-out spatially and temporally compared to the smooth surface due to wicking. Dry patches formed at the center of the channel which indicated wicking in the transverse direction (from the sidewalls inward). Wicking along the channel direction also existed since the dry patches formed earlier at downstream locations of the channel.

Fig. 8 The heat transfer performance characteristics of the microchannel. (a) The boiling curve (heat flux q'' *vs.* heater temperature rise ΔT). ΔT and q'' were calculated by equation (2) and (4) respectively. The red arrows indicate the CHF. (b) The HTC (calculated by equation (8)) as a function of q''. The error bars for q'' were approximately ±1%. The error bars for ΔT were approximately ±3.5 °C for the structured devices (shown for S4) and grew with the heat flux due to the increasing temperature oscillations (±3.5 °C to ±11 °C) for the smooth surface.

Fig. 9 Pressure drop across the microchannel as a function of heat flux for the devices investigated. The data were plotted until CHF. Error bars in

pressure were approximately ±430 Pa (shown for the smooth surface microchannel), which were calculated from the standard deviation of the temporal pressure measurement and the accuracy of the pressure transducers.

Fig. 10 The liquid wicking velocity u_{ave} as a function of the diameters d and pitches l of the micropillars, when the height h is fixed (h = 25 μm). u_{ave} is calculated by equation (10), and the magnitude of u_{ave} is proportional to the flow rate of the wicking liquid film in the pillar arrays. The symbols on the curves mark the locations of the geometries of the micropillars investigated in this study.

Table Caption List

Table 1 Geometric parameters (height, diameter and pitch) of the fabricated micropillars in the microchannel test devices.

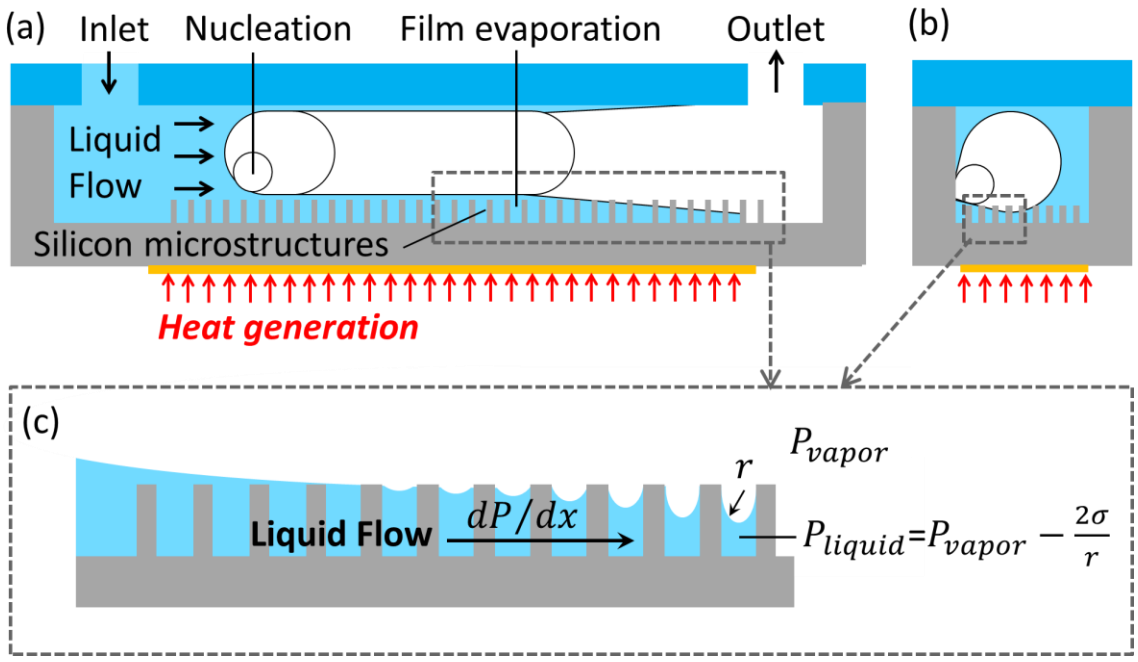

Figure 1. Schematic of the microchannel heat sink design with micropillars on the heated surface. (a) Side view, (b) cross-section view, and (c) magnified view of the liquid film forming menisci which create the capillary pressure gradient, *dP/dx*, that helps drive the liquid flow. The equation that describes the liquid pressure below the meniscus is the Young-Laplace equation where σ is the surface tension of the liquid, r is the radius of curvature of the local meniscus, and P_{liquid} and P_{vapor} are the local pressure of the liquid and vapor respectively.

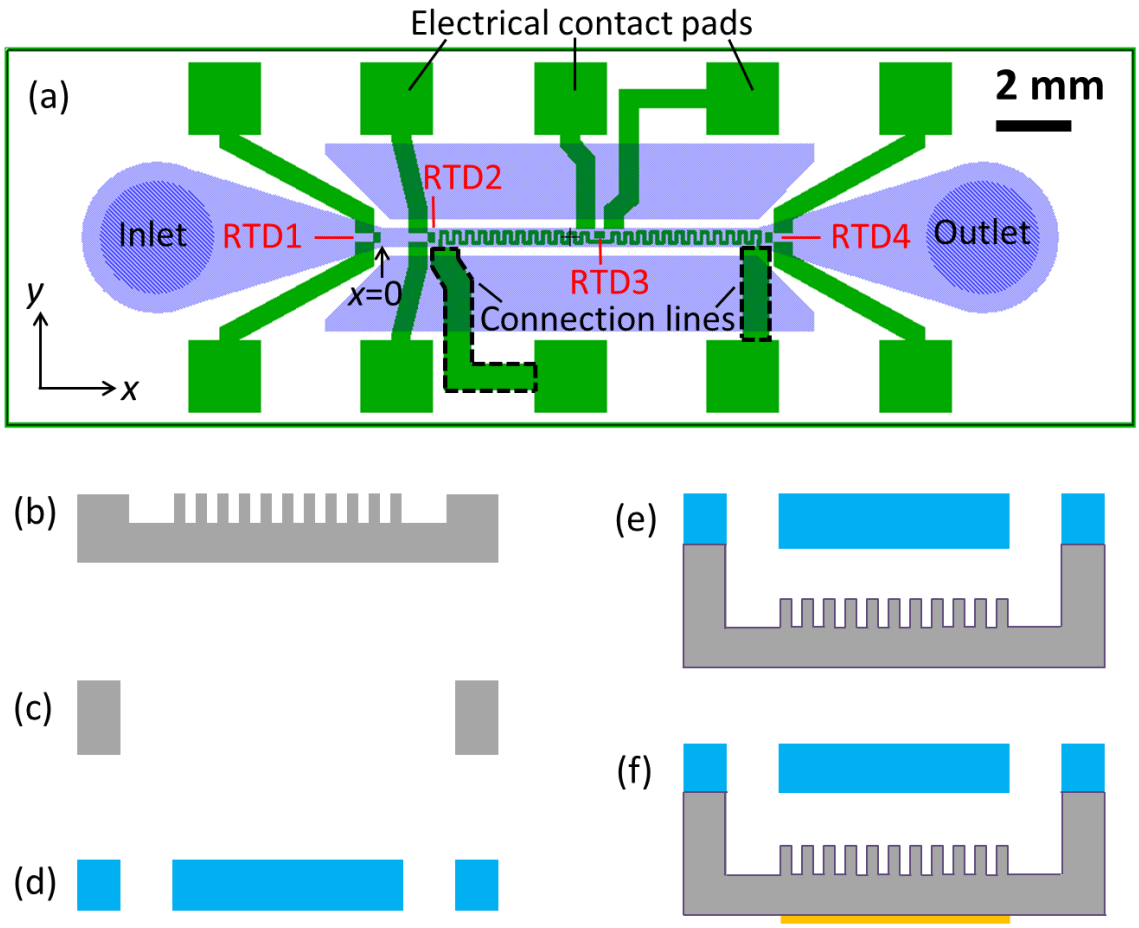

Figure 2. Design and fabrication process of the microchannel device. (a) Schematic (to scale) of the heater and RTDs on the backside of the microchannel device. The dotted sections are the electrical connection lines to the contact pads. (b) Micropillars of 25 μm height were etched in Si using deep reactive ion etching (DRIE). (c) A Si wafer was etched through using DRIE to define the channel. (d) Inlet and outlet ports were laser-drilled on a Pyrex glass wafer. (e) The Si layers were bonded using direct Si-Si bonding. A silicon dioxide (SiO_2) layer was thermally grown on the Si surface. The Pyrex layer was bonded to the top Si layer using anodic bonding. (f) A platinum (Pt) layer was deposited on the backside of the microchannel using electron-beam evaporation and patterned to form the heater and RTDs.

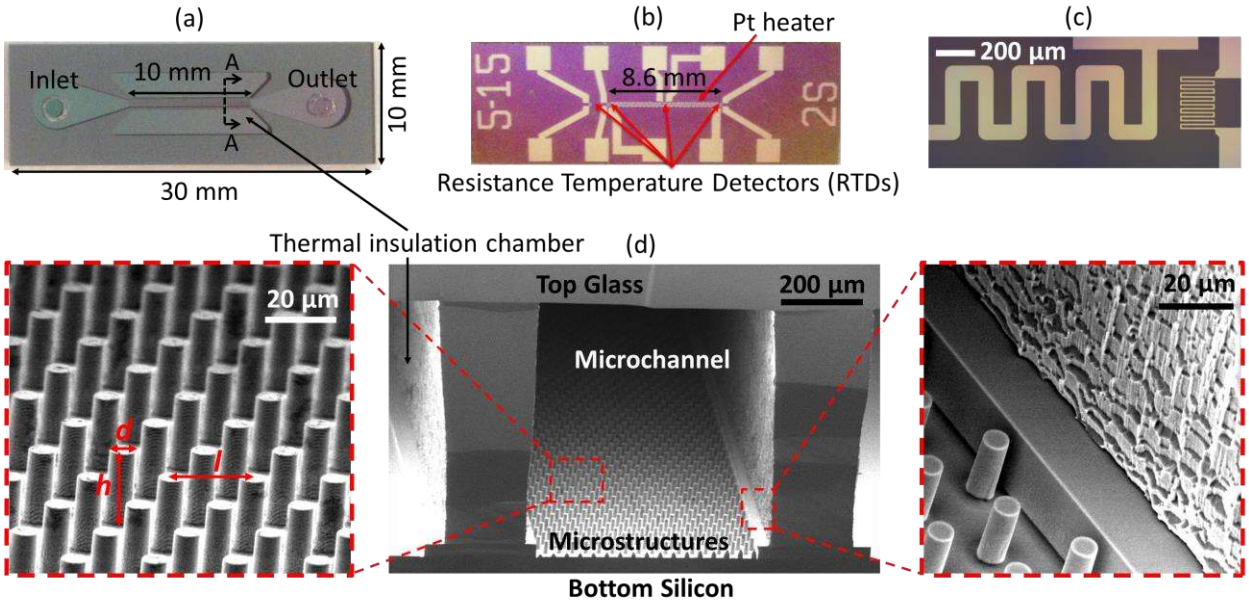

Figure 3. Images of a representative fabricated microchannel with micropillar arrays. Optical images of the (a) front and (b) backside of a device. (c) Optical microscope image of the heater and RTD4 on the backside of the microchannel. (d) SEM image of the cross section (A-A plane in 3a) of a microchannel with magnified view of the micropillars (left inset) and a sidewall at the bottom corner (right inset).

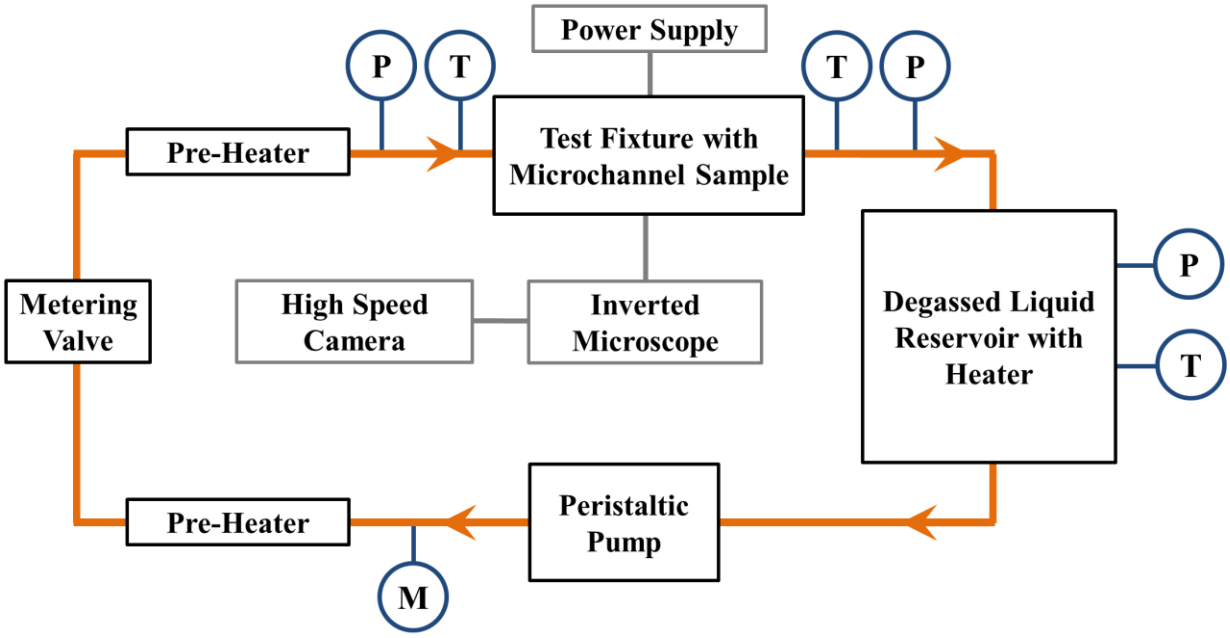

Figure 4. Schematic of the custom flow boiling loop used in the study. The loop consists of a liquid reservoir, a pump to provide a constant flow rate, a valve for flow stabilization, pre-heaters to minimize subcooling, a test fixture to interface with the test device, and various sensors. The components "P", "T" and "M" indicate locations of pressure transducers, thermocouples and the liquid flow meter respectively.

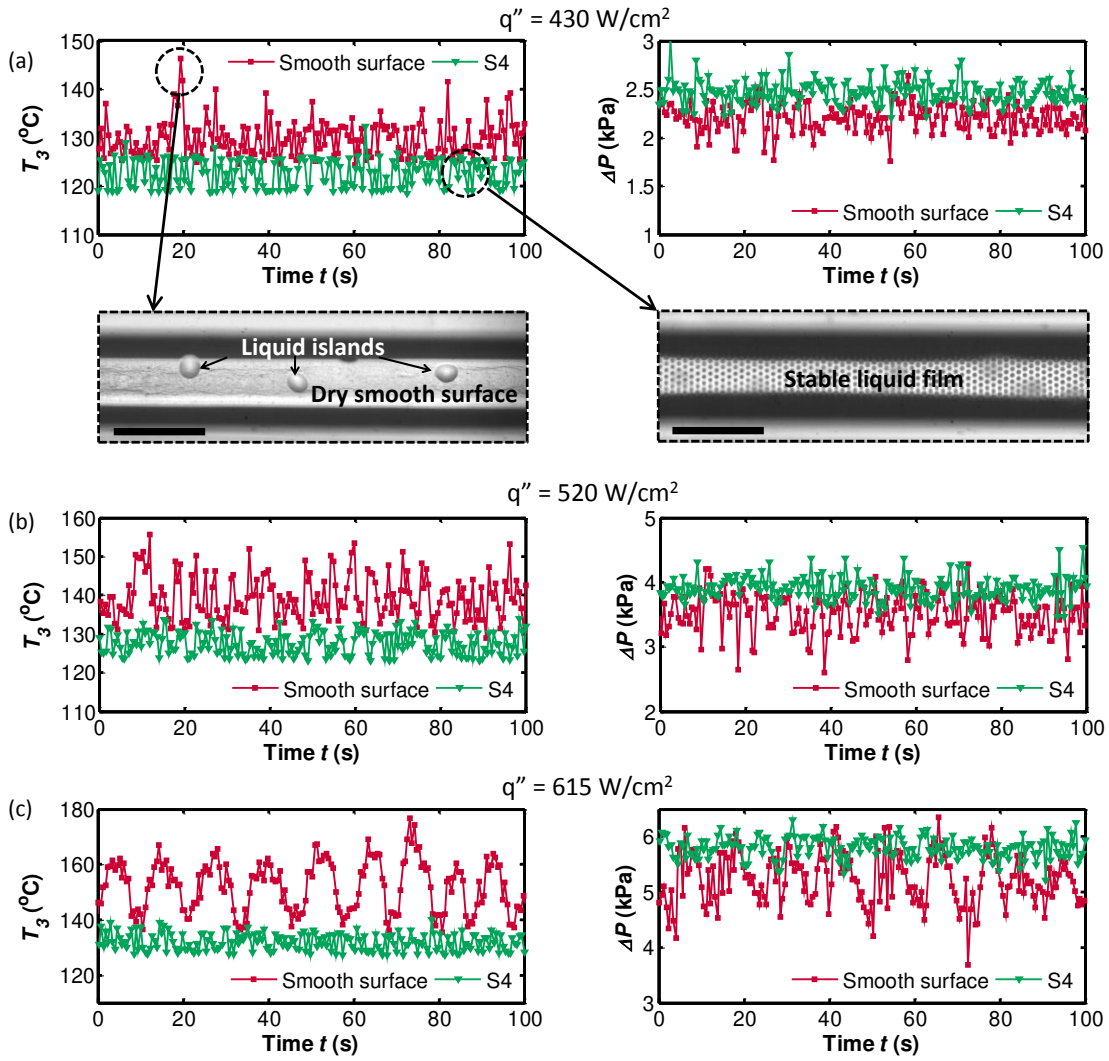

Figure 5. Temporally resolved temperature and pressure drop, and flow visualization at G = 300 kg/m^{2}s. (a) Mid-point backside surface temperature T_3 and pressure drop across a smooth surface microchannel and a structured surface microchannel S4 at q'' = 430 W/cm^2. Insets are optical images of a smooth bottom channel surface and a structured bottom channel surface (S4). Mid-point backside surface temperature T_3 and pressure drop of a smooth surface microchannel and a structured surface microchannel S4 at (b) q'' = 520 W/cm^2 and (c) q'' = 615 W/cm^2. The uncertainties of the temperature and pressure drop measurement were approximately ±2 °C and ±300 Pa.

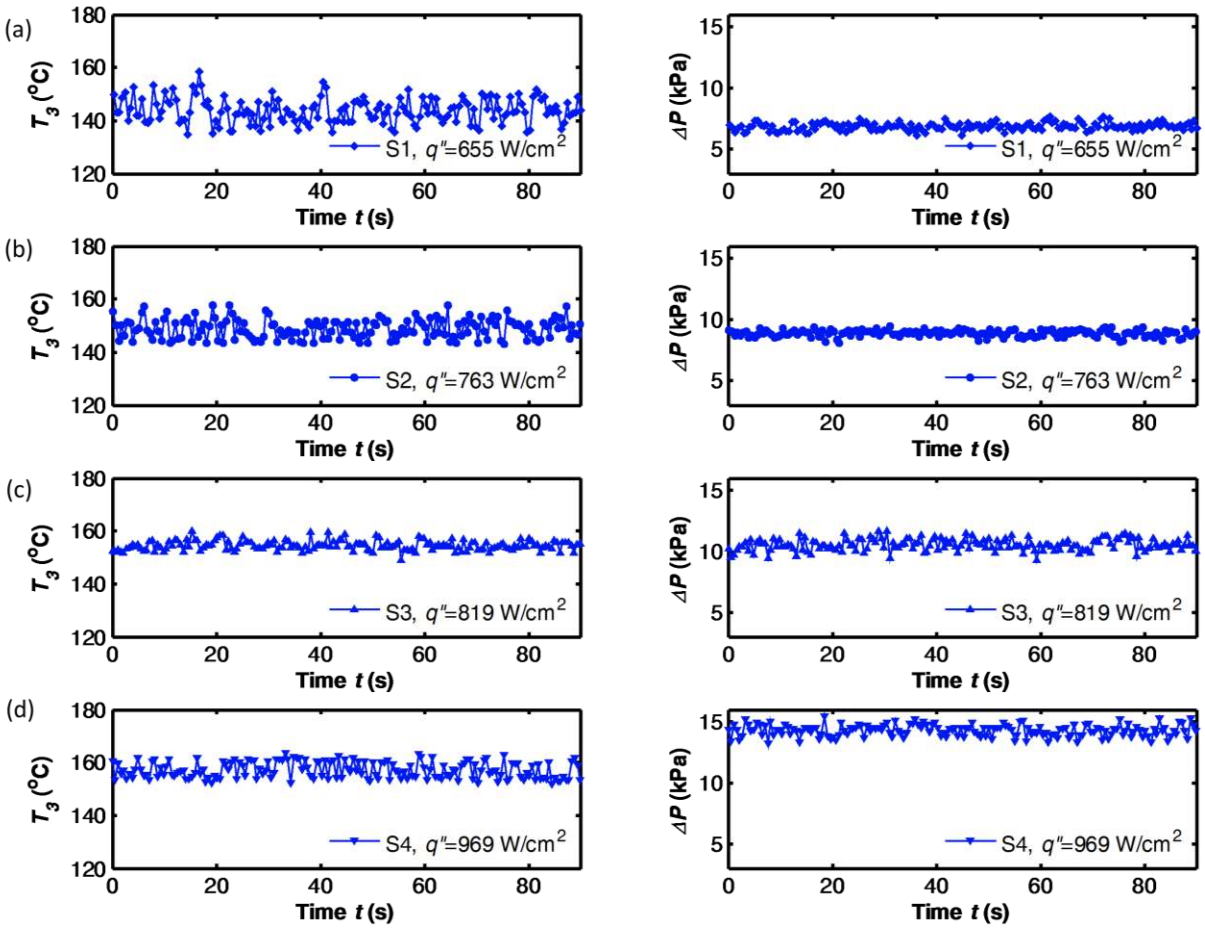

Figure 6. Mid-point backside surface temperature T_3 and pressure drop ΔP fluctuations of the structured surface microchannels at CHF (the highest heat flux beyond which dry-out occurred). (a) device S1 at q'' = 655 W/cm^2, (b) device S2 at q'' = 763 W/cm^2, (c) device S3 at q'' = 819 W/cm^2 and (d) device S4 at q'' = 969 W/cm^2. The mass flux G = 300 kg/m^{2}s. The uncertainties of the temperature and pressure drop measurement were approximately ±2 °C and ±300 Pa.

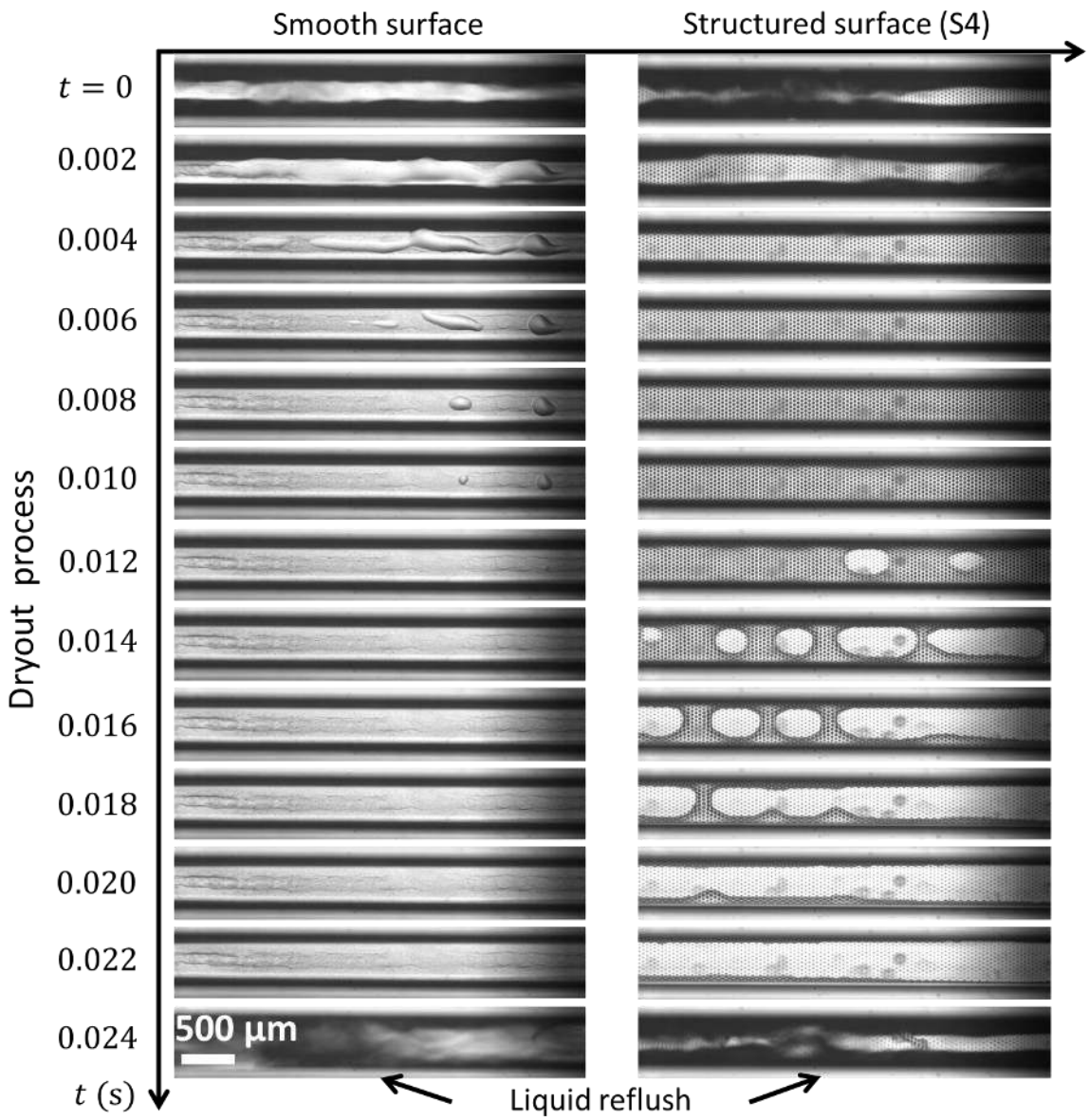

Figure 7. Time-lapse images of the dynamic dry-out process on a smooth surface and on a structured surface (S4) captured by a high speed camera. q'' = 430 W/cm^2 and G = 300 kg/m^{2}s. The structured surface showed less dry-out spatially and temporally compared to the smooth surface due to wicking. Dry patches formed at the center of the channel which indicated wicking in the transverse direction (from the sidewalls inward). Wicking along the channel direction also existed since the dry patches formed earlier at downstream locations of the channel.

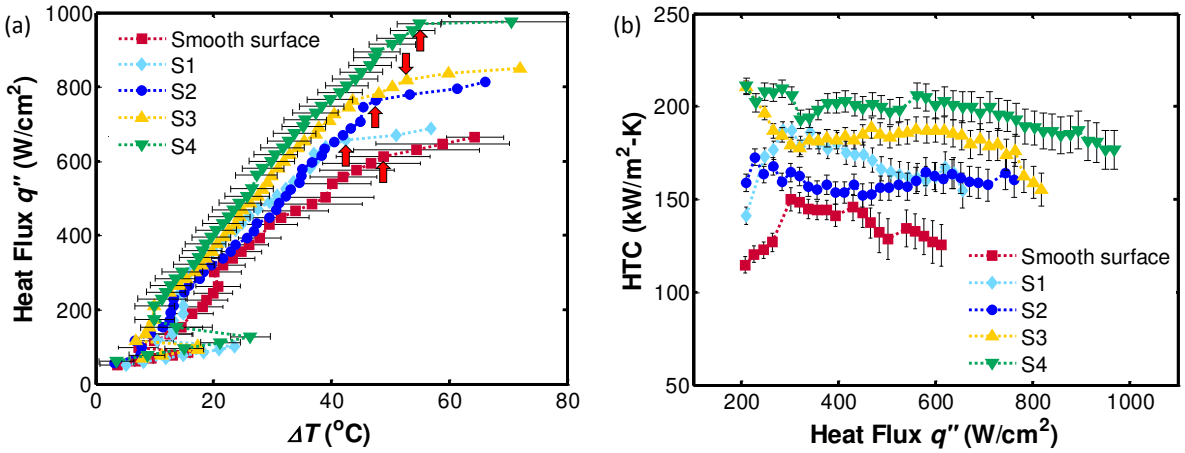

Figure 8. The heat transfer performance characteristics of the microchannel. (a) The boiling curve (heat flux *q"* *vs.* heater temperature rise ΔT). ΔT and *q"* were calculated by equation (2) and (4) respectively. The red arrows indicate the CHF. (b) The HTC (calculated by equation (8)) as a function of *q"*. The error bars for *q"* were approximately ±1%. The error bars for ΔT were approximately ±3.5 °C for the structured devices (shown for S4) and grew with the heat flux due to the increasing temperature oscillations (±3.5 °C to ±11 °C) for the smooth surface.

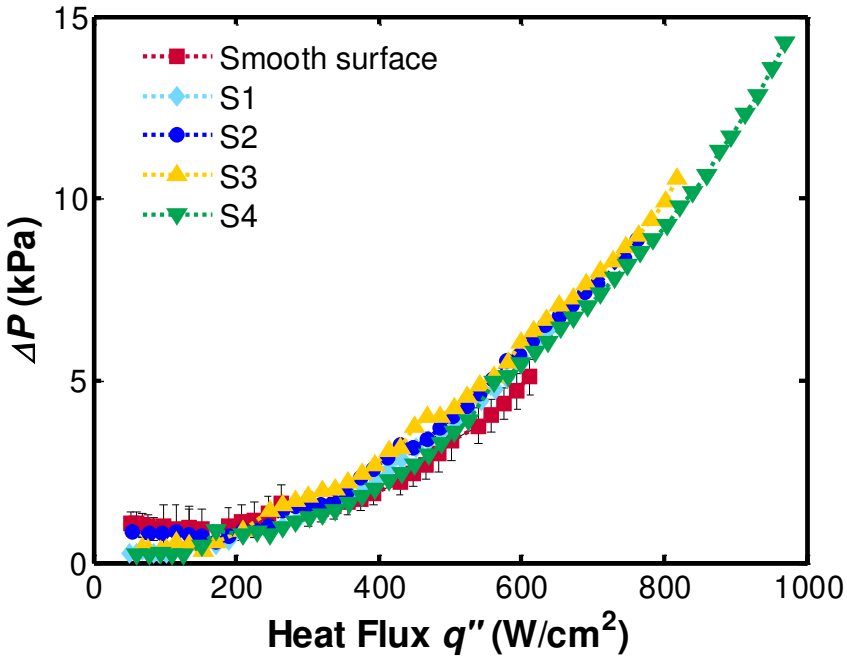

Figure 9. Pressure drop across the microchannel as a function of heat flux for the devices investigated. The data were plotted until CHF. Error bars in pressure were approximately ±430 Pa (shown for the smooth surface microchannel), which were calculated from the standard deviation of the temporal pressure measurement and the accuracy of the pressure transducers.

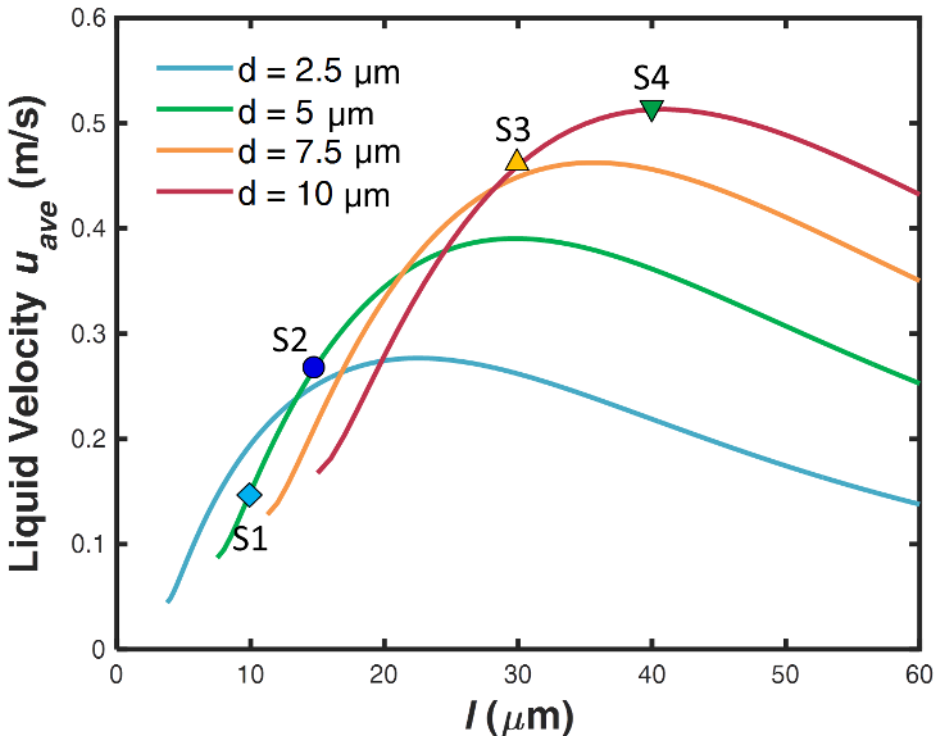

Figure 10. The liquid wicking velocity u_{ave} as a function of the diameters d and pitches l of the micropillars, when the height h is fixed (h = 25 μm). u_{ave} is calculated by equation (10), and the magnitude of u_{ave} is proportional to the flow rate of the wicking liquid film in the pillar arrays. The symbols on the curves mark the locations of the geometries of the micropillars investigated in this study.

Table 1. Geometric parameters (height, diameter and pitch) of the fabricated micropillars in the microchannel test devices.

Device No.	Height, h (μm)	Diameter, d (μm)	Pitch, l (μm)
S1	25	5	10
S2	25	5	15
S3	25	10	30
S4	25	10	40